Journal of Alloys and Compounds 910 (2022) 164724

Contents lists available at ScienceDirect

Journal of Alloys and Compounds

journal homepage: www.elsevier.com/locate/jalcom

Probing the structural evolution and its impact on magnetic properties of FeCoNi(AlMn)$_x$ high-entropy alloy at the nanoscale

C. Bazioti[a,*], O.M. Løvvik[a,b], A. Poulia[a], P.A. Carvalho[b], A.S. Azar[b], P. Mikheenko[a], S. Diplas[b], A.E. Gunnæs[a]

[a] Department of Physics, Centre for Materials Science and Nanotechnology, University of Oslo, P.O. Box 1048, Blindern, Oslo NO-0316, Norway
[b] Materials Physics-Oslo, SINTEF Industry, P.O. Box 124, Blindern, Oslo NO-0314, Norway

ARTICLE INFO

Article history:
Received 14 January 2022
Received in revised form 17 March 2022
Accepted 21 March 2022
Available online 25 March 2022

Keywords:
High-entropy alloys
Transmission electron microscopy
DFT calculations
Magnetic properties
Phase separation
Preferential site ordering

ABSTRACT

We report the first nanoscale investigation of FeCoNi(AlMn)$_x$ high-entropy alloys (HEAs) processed by laser metal deposition. The structural evolution of the alloy upon chemical composition variation ($0.2 \le x \le 1.5$) was investigated by combining imaging and spectroscopies in (scanning) transmission electron microscopy (S)TEM with density functional theory (DFT). A gradual change from a face-centered cubic (FCC) towards an ordered full-Heusler ($L2_1$) phase by increasing the Al and Mn contents was observed. Direct imaging and atomic-scale calculations revealed a nanoscale interplay between B2 and $L2_1$ ordered structures for x = 1.5, wherein the latter, Al and Mn occupy two different Wyckoff sites. By decreasing x, the FCC phase dominates exhibiting intense phase separation tendency, ordering phenomena, and nano-precipitation. Although not chemically discriminated, plasmon-peak splitting in low-loss electron energy loss spectra revealed the presence of two valence electron densities within the FCC phase. Lorentz TEM showed that the ordered nano-precipitates and nano-sized grains with a structure based on a tripled FCC unit cell are pinning-sites for magnetic domain walls and dislocations. All alloy compositions exhibited soft-magnetic behavior with coercivity (H_c) values < 1000 A/m. The FeCoNi(AlMn)$_{1.5}$ alloy with $L2_1$/B2 nanostructure showed the highest magnetization (M_s) with relatively low H_c, attributed to the large magnetic moment of Mn and the synergistic effect of Mn-Al according to DFT, whilst ordering does not impose a negative effect. Phase separation trends within the FCC phase seem to decrease the M_s however, the overall impact on the magnetic behavior is not intense, opening up for new avenues for tuning FeCoNiAlMn properties through chemically-designed phase decomposition regimes.

1. Introduction

Since 2004, when the conception of high-entropy alloys (HEAs) was first brought up [1,2], this new class of materials has become one of the hotspots of scientific interest due to their intriguing properties. HEAs are multi-component systems consisting of 5 or more elements [3,4] and exhibit the potential to stabilize chemically-disordered single-phase solid solutions (SS) by high configurational entropy (S_{config}) [5–9] - instead of chemically-ordered intermetallic phases (IM) which are stabilized by a high enthalpy of formation. Despite early reports, the requirement for equimolar elemental concentrations proved to be unnecessarily restrictive and HEAs are now predicted to be formed within a compositional range of 5–35 at% of the principal elements [1,10]. Due to this wide compositional flexibility, HEAs offer a promising landscape to explore and optimize material development, as well as tune their properties in a controlled way [11–13]. So far, in addition to the excellent reported mechanical performance [14–21], HEAs are also ideal candidates for achieving soft magnetic properties and superconductivity [22–25]. Soft magnets are important in electrical systems used in power generation, electromagnets, and transmission [26]. The FeCoNiAlMn system is a promising candidate for a soft magnet material and recently high saturation magnetization (M_s) and low coercivity (H_c) values have been reported [27–34].

The magnetic properties of an alloy are sensitive to the base-alloy, the extra alloying additions, and the crystal structures of the resulting phases [35–43]. In particular, M_s depends on chemical composition, atomic-scale structure, and phase constitution [44], while H_c is affected by grain size, presence of defects, impurities, and internal stresses [45]. In addition to the high entropy effect, other

* Corresponding author.
E-mail address: kalliopi.bazioti@smn.uio.no (C. Bazioti).

https://doi.org/10.1016/j.jallcom.2022.164724
0925-8388/

parameters such as enthalpy of mixing (ΔH_{mix}), atomic size mismatch (δ), elastic-strain energy (ΔH_{el}), and valence electron concentration (VEC) can also play a role in phase stability, making the alloys vulnerable to phase decomposition [46–53]. Phase stability in multicomponent systems is complicated and depends on the interplay of phase separation and ordering. These phenomena involve spinodal decomposition leading to nanoscale-modulated structures, chemical segregation at grain boundaries (GBs) resulting in spatially-confined spinodal decomposition and ordered superstructures, formation of nano-precipitates, etc. [54–62]. Hence, it is of utmost importance to unravel the structure of the alloys not only at the micro- but also at the nano-scale, to select the appropriate compositional range and optimize their synthesis. The most common phases identified in HEAs are the chemically-disordered FCC ($Fm\bar{3}m$) and BCC ($Im\bar{3}m$) followed by the chemically-ordered B2 [11]. The B2 phase resembles an 'ordered BCC' phase, where A and B atoms occupy the Wyckoff positions 1a (0, 0, 0) and 1b (½, ½, ½) respectively. A commonly ordered derivative of the B2 phase is the full-Heusler $L2_1$ ($Fm\bar{3}m$) where A, B, and C atoms occupy the Wyckoff positions 4a (0, 0, 0), 4b (½, ½, ½) and 8c (¼, ¼, ¼) respectively [63].

Recently, a systematic study of $FeCoNiAl_xMn$ and $FeCoNi(AlMn)_x$ was conducted experimentally by Hariharan et al. [32], Zuo et al. [64] and Li et al. [29] and theoretically by Feng et al. [40], showing the dependence of magnetic properties on phase changes triggered by tuning the alloy composition. A phase transition from FCC to BCC/B2 was revealed by increasing x, with the equimolar FeCoNiAlMn exhibiting the highest M_s. So far, most of the structural studies have been conducted on the micro-scale, by combining X-ray diffraction (XRD) and scanning electron microscopy (SEM). Although these methods provide information on the stabilization of the dominant phases, they cannot detect phenomena occurring at the nanoscale, and this potentially leads to misinterpretation of mechanisms affecting alloy properties.

Here, we report on the first atomic-level investigation of $FeCoNi(AlMn)_x$ ($0.2 \leq x \leq 1.5$) prepared by the additive manufacturing technique of laser metal deposition (LMD) [65–68], combining advanced experimental characterization and theoretical analysis. Amongst other advantages, additive manufacturing enables the production of items with complex shapes such as those found in applications requiring magnets with internal channels for cooling purposes. Micro- and nano-scale investigations were performed by SEM and XRD along with (scanning) transmission electron microscopy ((S)TEM) combined with energy-dispersive X-ray spectroscopy (EDX) and electron energy loss spectroscopy (EELS). Quantum mechanical modeling using density functional theory (DFT) was used to assess the relative stability of different structural models of selected compositions, giving support and adding detail to the experimental studies. A comparative study was conducted by varying the Al and Mn content (x) at the same time and results of three representative cases are presented: ~ 6, 15, and 25 at%, satisfying the compositional requirements for HEAs. The corresponding impact on the magnetic properties was investigated by vibrating sample magnetometer (VSM) and Lorentz TEM.

2. Materials and methods

$FeCoNi(AlMn)_x$ ($0.2 \leq x \leq 1.5$) alloys were processed by LMD through the weight-controlled blending of elemental powders. The processing conditions and parameters were kept identical for all samples [69]. At the alloy design stage, various geometrical and thermodynamic parametric models were used to predict phase evolution in the system. It was thus suggested that (among others) the minimum requirements for single solid solution (SS) phase formation are i) the atomic size parameter (γ), which takes into consideration the atomic packing misfit in multicomponent systems, should be below 1.175. γ is defined as $\gamma = \left(1 - \sqrt{\frac{(r_S+\bar{r})^2 - \bar{r}^2}{(r_S+\bar{r})^2}}\right) \Big/ \left(1 - \sqrt{\frac{(r_L+\bar{r})^2 - \bar{r}^2}{(r_L+\bar{r})^2}}\right)$, where r_L and r_s are the radii of the largest and smallest atoms [70] and ii) the parameter Φ should be above 1. Φ is defined as $\Phi = \Delta G_{ss}/|\Delta G_{max}|$, where ΔG_{ss} is the change in Gibbs free energy of formation for a fully disordered SS consisting of the individual elements. ΔG_{max} is the lowest (intermetallic) or highest (segregated) possible Gibbs free energy of formation for the various binary systems between the constituents of the mixture. Negative Φ values indicate that SS will not be formed, owing to positive formation enthalpy [71]. The calculated values of the above-mentioned parameters for the actual compositions of the produced alloys suggested that all three samples will have a phase separation tendency rather than forming a single SS. In particular, γ was ranging at the limit of its proposed value for samples with x = 1.5 and x = 0.65 or slightly higher for x = 0.2, and parameter Φ was far below 1 for all three samples. Thus, the prediction models gave a first indication that the structure of the alloys would be complicated, consisting of more than one phase.

Microstructural characterization was performed using an FEI Nova NanoSEM 650 equipped with EDX and an electron backscattered diffraction (EBSD) system, while the crystal structure of the powder materials was analyzed by XRD employing a Rigaku MiniFlex600 system using Cu Ka radiation and fluorescence correction.

Atomic-scale investigations were conducted on an FEI Titan G2 60–300 kV microscope, combining (S)TEM, EDX, and EELS. The microscope is equipped with a CEOS DCOR probe-corrector, monochromator, and Super-X EDX detectors. Observations were performed at 300 kV with a probe convergence angle of 24 mrad. The camera length was set to 60 mm and simultaneous STEM imaging was conducted with 3 detectors: high-angle annular dark-field (HAADF) (collection angles 101.7–200 mrad), ADF (collection angles 22.4–101.7 mrad), and annular bright-field (ABF) (collection angles 8.5–22.4 mrad). The resulting spatial resolution achieved was approximately 0.08 nm. EELS was performed using a Gatan Quantum 965 imaging filter. The energy dispersion was 0.1 eV/channel and the energy resolution measured using the full width at half maximum (FWHM) of the zero-loss peak was 1.1 eV. Electron transparent TEM samples were prepared by mechanical grinding and polishing (Allied MultiPrep) as well as with an FEI Helios G4 Dual-beam using Ga ion beams FIB. Final thinning was performed by Ar ion milling with a Fishione Model 1010, and plasma cleaning was applied directly before the TEM investigations, with a Fishione Model 1020.

A Lake Shore PMC MicroMag 3900 VSM was used for the analysis of the magnetic properties of the samples through measurements of the magnetic hysteresis loops with direct current magnetization as a function of the applied magnetic field up to 1.5 T.

Electronic-scale calculations based on density functional theory (DFT) were performed with the Vienna Ab initio Simulation Package (VASP) [72,73] where the PBE [74] generalized gradient approximation was employed. Solid-solution structures were simulated with special quasirandom structures (SQS) [75] consisting of 48 atoms, generated with the temperature-dependent effective potential (TDEP) [76] software. Five different SQS candidates were tested for each composition and model. Energies were converged within 1 meV per formula unit and forces within 0.01 eV/Å concerning VASP numerical parameters (plane-wave energy cutoff 500 eV, overall precision Accurate, self-consistency energy change criterion 10^{-6} eV, **k**-point density of at least 4 points per reciprocal Å). To keep a cubic primitive unit cell, structural relaxations were performed with fixed angles while volume and atomic positions were allowed to relax. Each relaxation was restarted before a final static calculation was performed on the relaxed structure. Magnetic calculations were initiated by magnetic moments equal to 0 or 2 Bohr magnetons for each atom, corresponding to the different magnetic orderings.

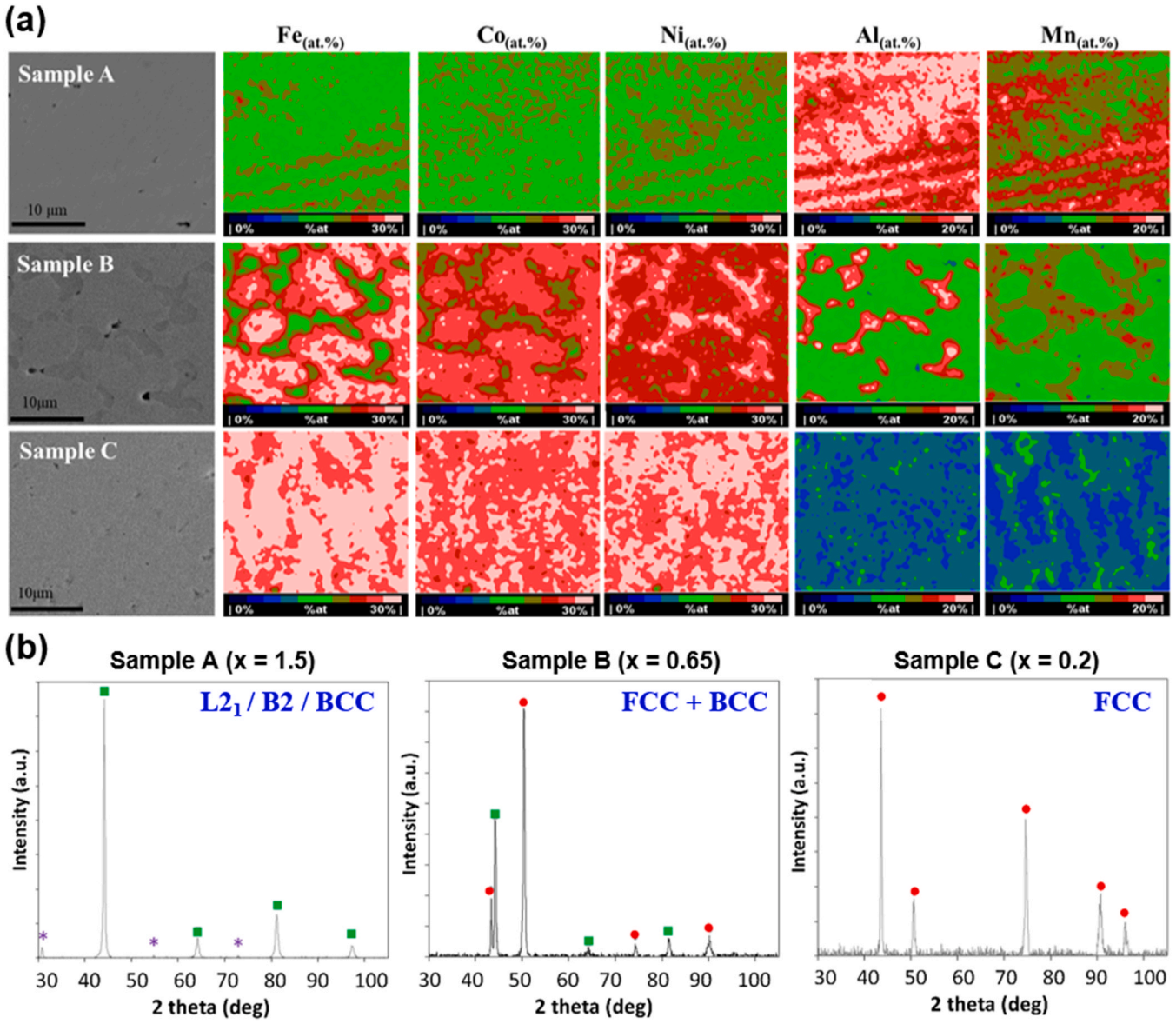

Fig. 1. a) SEM images and the corresponding EDX quantified maps and b) XRD patterns of Samples A, B, and C. A gradual change from FCC towards an ordered BCC-based structure by increasing the Al, Mn content is revealed (from Sample C to A). At intermediate compositions (Sample B) the alloy exhibits a dendritic microstructure, with the dendrites being FCC as shown by TEM in §3.2.

Ferromagnetic, nonmagnetic, and antiferromagnetic/ferrimagnetic orderings were separately relaxed and their total energy compared. The configurational entropy was calculated using Boltzmann's distribution from the number of possible microstates and Sterling's approximation to handle the factorials.

3. Results

3.1. Microstructural characterization by SEM/EDX and XRD

Fig. 1. illustrates a) SEM/EDX and b) XRD results of Samples A (x = 1.5), B (x = 0.65) and C (x = 0.2). For the high Al, Mn contents (Sample A), XRD revealed diffraction peaks that could be attributed to the {110}, {200}, {211}, and {220} crystal planes of the BCC phase (green square symbol). In addition, extra reflections were observed indicating the existence of ordering (purple star symbol). The first one at ~ 31° could be attributed to the superlattice reflection peak that corresponds to the {100} planes of the ordered B2 phase or the {200} planes of the Heusler ($L2_1$) phase. However, XRD cannot reveal whether the alloy is a single ordered phase ($L2_1$ or/and B2) or a mixture of both ordered and disordered BCC, hence detailed information was extracted by TEM (see §3.2). Chemical inhomogeneities of up to ~6 at% were detected. In particular, grains enriched in Fe/Mn and depleted in Al/Ni were observed; however, they were not a dominant feature. Reduction of the Al, Mn content (Sample B) leads to the formation of dendritic microstructure. The dendrites exhibit an average composition value of x ~10 at%, while the inter-dendritic regions are enriched in Al, Mn, and Ni. XRD revealed the coexistence of an FCC (red circle symbol) phase and a BCC phase. However, TEM (in §3.2) showed that the dendrites have an FCC crystal structure while the interdendritic regions are $L2_1$. By a further reduction in the Al, Mn content (Sample C), the FCC phase prevails resulting in a single-phase alloy with relatively good chemical homogeneity (chemical variations up to 3 at%) and x reaching an average value ~5 at%.

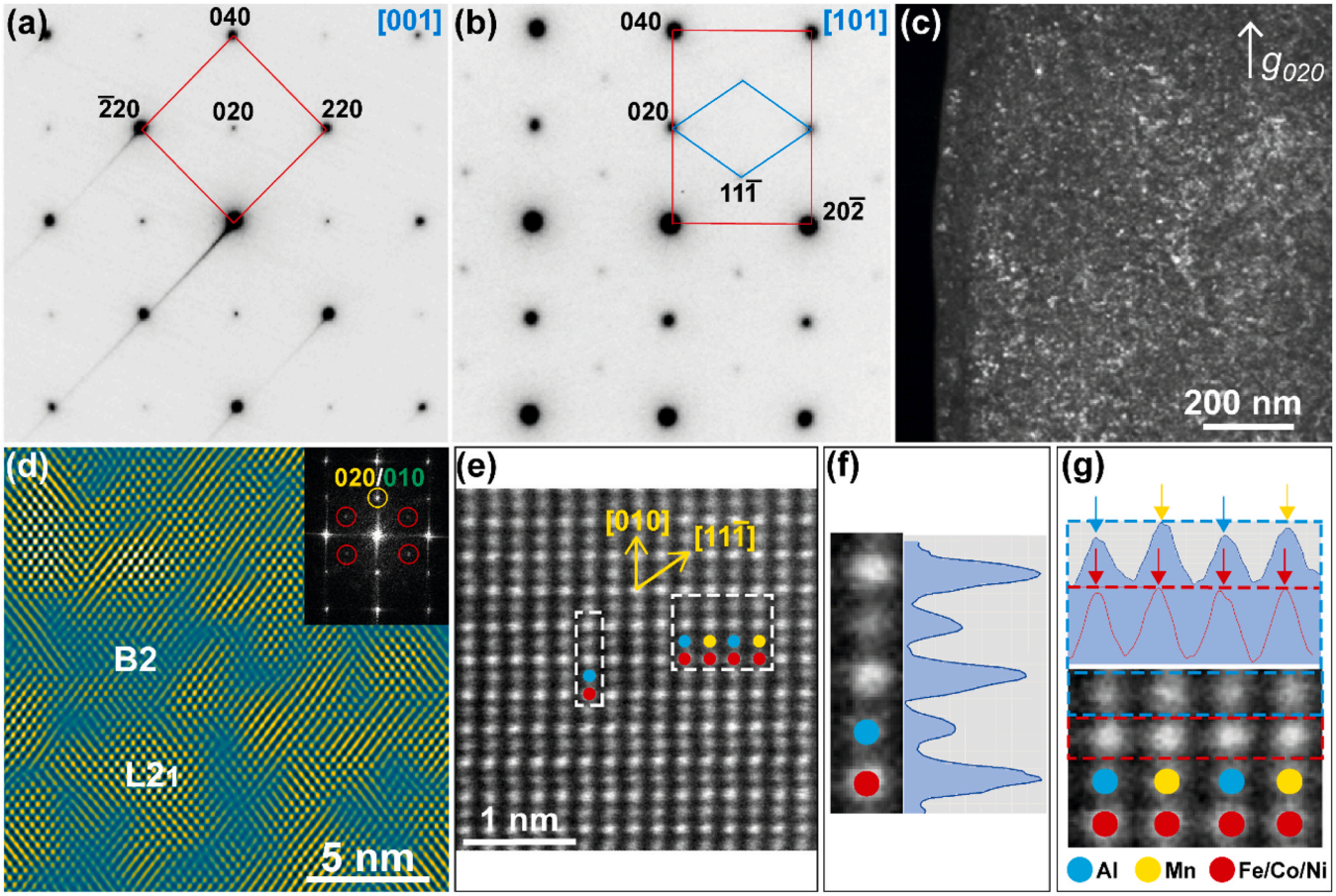

Fig. 2. Nanoscale interplay between ordered B2 and $L2_1$ revealed for high Al and Mn contents (Sample A). a) SAED pattern along the [001] direction. Intensity change of diffracted peaks is detected, indicative of ordering (the indexing is done according to $L2_1$, however, the superlattice 020 reflection could also correspond to 010 of B2). b) SAED pattern along the [101] direction. The Heusler structure is verified by the {111} reflections. c) Two-beam dark-field (DF) image using the g020 (or g010) superlattice reflection, showing homogeneous distribution of ordering at the micro-scale. d) Bragg filtered high-resolution STEM image acquired from an ordered area using the {111} $L2_1$ reflections (annotated by red circles in the FFT inset). Nanoscale interplay between $L2_1$ (yellow) and B2 (green) ordering is detected. e) High-resolution HAADF-STEM image along the [101] direction and f)-g) close-ups with intensity profiles, showing ordering along the (202) and (020) planes. In conjunction with the DFT model presented in §3.3, Al and Mn occupy the a and b Wyckoff sites respectively, while Fe, Co, Ni occupy the c sites.

3.2. Nano-scale characterization by (S)TEM-EDX-EELS

3.2.1. Phase identification - atomic site occupancy – phase separation

In addition to the information extracted at the meso-scale, detailed (S)TEM, EDX, and EELS analysis at the nano-scale revealed a more complicated structural picture. Starting with Sample A, Figs. 2a and 2b show selected area electron diffraction (SAED) patterns along different sample orientations. Clear ordering was observed that is mainly attributed to a Heusler phase due to the {111} superlattice reflections detected along with the [101] orientation. However, there were areas where these reflections were not detected (or were very weak) indicating that B2 ordering also exists. To understand the spatial extension and distribution of each phase, a thorough analysis comprising two-beam imaging in TEM and Bragg-filtering of high-resolution STEM images was conducted. Fig. 2c illustrates a dark-field TEM image recorded under two-beam conditions with the superlattice reflection g020 of Heusler (or g010 of B2). No signs of phase separation at the micro-scale are observed, in contrast to Zuo et al. [36] who detected under the same imaging conditions BCC nanoparticles embedded in B2 matrix for equimolar FeCoNiAlMn. Our variations in contrast are attributed to the presence of nano-scale stresses of the alloy. Fig. 2d shows a Bragg filtered high-resolution STEM image acquired from an ordered area using the g111 Heusler reflection (annotated by red circles in the fast Fourier transform (FFT) inset). A nanoscale interplay between Heusler (yellow) and B2 (green) ordering is detected. Direct observation of the atomic structure and ordering was achieved by performing high-resolution HAADF-STEM imaging along the [101] direction (Fig. 2e). Along this projection, atomic species occupy separate atomic columns and since in HAADF the contrast depends on the atomic number Z, an initial chemical identification can be postulated. The full occupancy of all atomic columns reveals that we have indeed a B2 or full-Heusler structure ($L2_1$), and not a half-Heusler structure. Furthermore, since Al has lower Z in comparison to the other metallic constituents, it can be postulated that the planes of lower Z-contrast are mainly occupied by Al (Fig. 2f). Ordering along these planes could be detected easily (Fig. 2g, blue intensity profile), due to the large Z-difference between Al and transition metals (Mn, Fe, Co, Ni). The red intensity profile from the next plane could not detect any periodical trend. This indicates that these planes are mainly occupied by transition metals (Fe, Co, Ni), and due to their small difference in Z, intensity changes are not easily detectable. Hence, we can postulate that Al and Mn occupy the a and b Wyckoff sites of the Heusler superlattice, while Fe, Co, Ni occupy the c sites (further predicted by DFT in §3.3).

By decreasing the x content of the alloy (Sample B), STEM imaging (Fig. 3a) revealed the existence of two distinct areas: a dominant 'matrix' (dendrite) and secondary 'embedded' areas that exhibit lower contrast (interdendritic regions). SAED patterns and FFTs targeting the two areas separately revealed that the dominant phase

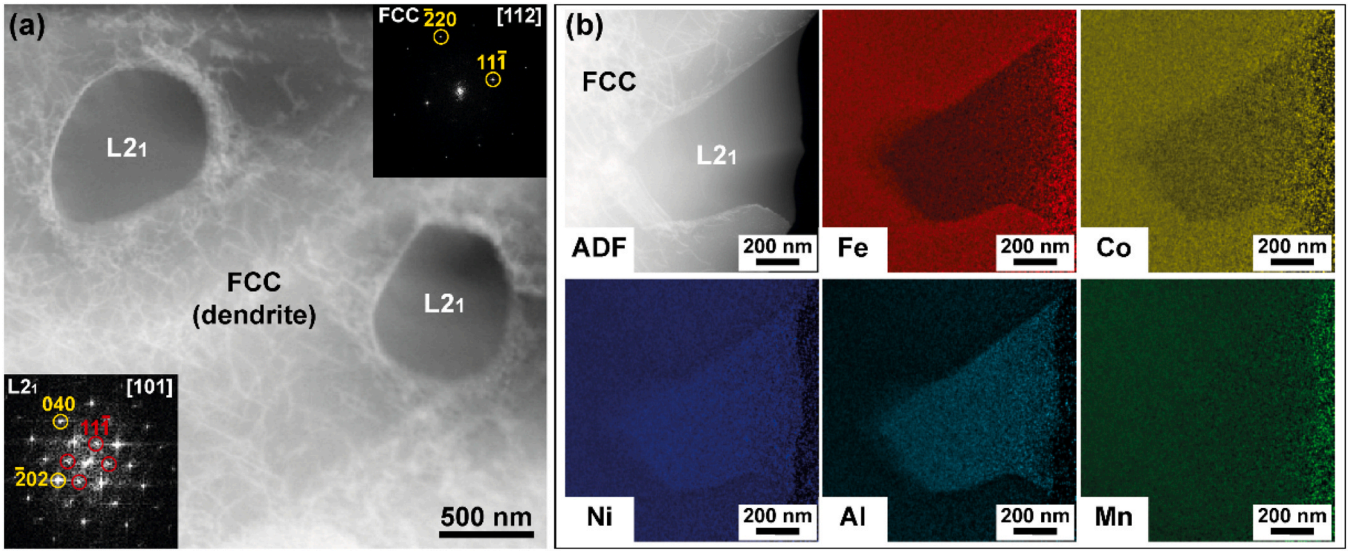

Fig. 3. a) ADF-STEM image and the corresponding FFTs (insets) illustrating both the dendritic (FCC) and interdendritic ($L2_1$) areas in Sample B. Due to the intense diffraction contrast, a dense network of dislocations is visible in the FCC dendritic phase, while the interdendritic $L2_1$ phase is almost defect-free. b) EDX quantified maps revealing an Al, Ni-richer $L2_1$ phase in comparison to the FCC dendrite.

Table 1
Unit cell size and chemical quantification by EDX-STEM.

Sample	A FeCoNi$(AlMn)_{1.5}$	B FeCoNi $(AlMn)_{0.65}$		C FeCoNi $(AlMn)_{0.2}$	
Phase	$L2_1$ dominant	FCC dendrite	$L2_1$ interdendrite	FCC dominant	Ordered Superstructures
Unit cell (nm)	0.6	0.37	0.6	0.37	3 × 0.37
Fe at%	17.1	29.2	19.5	29.3	26.3
Co at%	16.2	26.5	22.1	29.4	30.7
Ni at%	17.2	24.3	28.9	31.0	31.0
Al at%	24.4	07.1	16.8	06.0	01.7
Mn at%	25.2	12.9	12.8	04.3	10.4

was FCC, while the secondary phases were $L2_1$ (again as in Sample A, it could be an interplay between B2/ $L2_1$). The FCC phase exhibited a strong tendency for phase separation revealed by the intense moiré fringes observed in high-resolution images. Furthermore, this area exhibited a high density of defects as clearly illustrated in Fig. 3a. On the other hand, the Heusler $L2_1$ was defect-free with no indication of phase separation. EDX results (Fig. 3b) showed that these structurally-different areas also exhibited different chemical compositions. Chemical quantification showed that the $L2_1$ phase was Al, Ni-richer in comparison to the FCC dendrite (the results of the quantification are presented in Table 1).

Further decrease in x (Sample C) resulted in total elimination of the Heusler $L2_1$ structure and only the FCC phase was observed. The calculated lattice constants revealed a cubic unit cell with a = 0.37 nm. However, the FCC phase exhibited intense phase separation tendency (same as in the FCC phase in Sample B) as well as ordering trends. The SAED pattern in Fig. 4a for Sample C reveals a splitting of 220 reflections along the [110] direction (red arrows) and superlattice reflections, indicative of an ordered phase with three-times larger unit cell. High-resolution TEM images in Figs. 5a and 5b show that phase separation takes place at the nanoscale, resulting in intense moiré fringes only at the FCC phase, while it disappears at the ordered grains. The ordered grains were up to ~500 nm in size, while smaller ordered nano-precipitates down to ~5 nm were also detected. EDX shows that the ordered areas are slightly Mn, Co-richer (Fig. 4b) and exhibited lateral coherency with the FCC phase, with interfaces forming nano-steps. (Fig. 5c).

The phase separation trend was also examined by employing low-loss EELS. A comparative study was conducted, acquiring spectra from all different phases in the three samples. Careful determination of the plasmon peak position took place by applying dual-EELS, acquiring simultaneously the zero-loss and the plasmon peak regions. All plasmon peak spectra were aligned to the zero-loss peak to eliminate possible energy drifts during acquisition hence, to improve the precision in the evaluation of the plasmon peak position. Results showed that the FCC phases in both Samples B and C exhibited a splitting of the plasmon peak ~ 4.2 eV, indicating VEC = 2. This is consistent with the observed phase separation trend, indicating that each peak could be representative of each of the two overlapping phases. On the contrary, all ordered phases exhibited a single sharp plasmon peak (Sample A $L2_1$/B2, Sample B $L2_1$, Sample C ordered superstructures). A gradual blue shift was observed for decreasing x, indicating a relationship of the chemical content of the alloy with the energy position of the plasmon (Fig. 6).

3.2.2. *Pinning of magnetic domain walls and dislocations*

To study the impact of the ordered grains observed in FCC (Sample C), Lorentz TEM was employed in Fresnel-mode. Fig. 7 presents Lorentz TEM images of the ordered grain that was previously described (Figs. 4 and 5). By changing the defocus-sign, magnetic domain walls can be identified by the alternating contrast (bright-dark). These results showed that the ordered grains, as well as the small aluminum oxide inclusions, exist at the intersection of four magnetic domain walls, hence acting as pinning points for magnetic domain wall movement.

Furthermore, ordered nano-precipitates in FCC were found to act as pinning points for the movement of dislocations. In Fig. 8a, a low-magnification TEM image from Sample C shows dislocations pinned by nano-sized precipitates. A close-up of the area (Fig. 8b) indicates a clear connection of the precipitate with the dislocation line. This

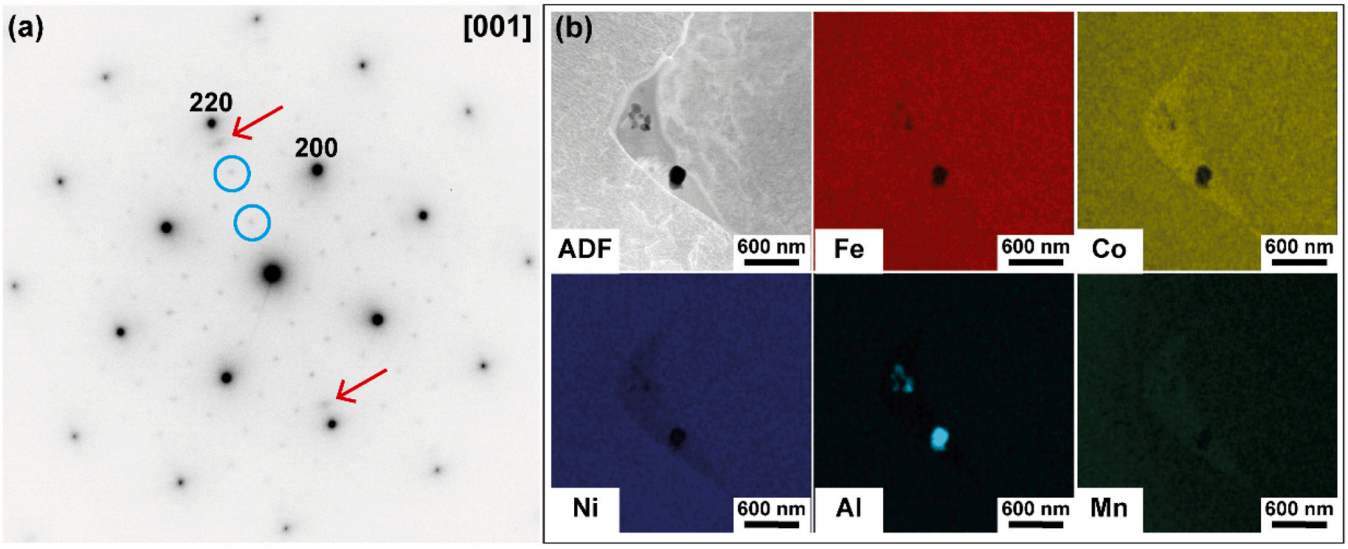

Fig. 4. a) SAED pattern along the [001] zone axis in Sample C. In addition to the FCC dominant phase, ordered areas with a three-times larger unit cell are detected (blue circles annotate the superlattice reflections). Furthermore, splitting of the 220 reflections is detected due to phase separation trends (annotated by red arrows). b) EDX quantified maps from an ordered superstructure. ADF-STEM illustrates a nano-sized grain in the middle of the image exhibiting ordering, formed at the grain boundary of two FCC grains. The ordered area is slightly Mn, Co-richer (see Table 1). Nanosized inclusions of aluminum oxides are also detected.

area was approximately 50 nm in size and was reaching an equilibrium shape defined by sharp facets, mainly formed at the (020) planes of the FCC phase. A high-resolution TEM image (Fig. 8c) from a similar nano-precipitate with the corresponding FFTs, clearly show nano-scale ordering. The corresponding inverse FFT (IFFT) image after applying masks at the superlattice reflections can be seen in Fig. 8d. Fig. 8e and Fig. 8f are close-ups of the FCC and the ordered regions, respectively. The ordered nano-precipitates exhibit lateral coherency with the surrounding FCC matrix while ordering results in a three-times larger cubic unit cell.

3.3. Calculated thermodynamic and magnetic properties

Simulation of the solid-solution phases with composition according to Table 1 was performed with 48-atom SQS models. Each atom thus corresponds to 2.08 at% of the supercell, which limits the compositional precision. Nevertheless, all models exhibited a composition less than 1 at% away from the experimental target composition, as shown in Table 2.

For each of the compositions, a number of different atomistic models were constructed, to corroborate the experimental structures. A few different alternative distributions of atoms over the Wyckoff sites were also included in the modeling, to complement the experiments in situations with low element contrast in the diffraction studies. This is outlined in Table 3. The DFT calculations were used to compare the formation enthalpy of ferromagnetic, nonmagnetic, and antiferromagnetic/ferrimagnetic ordering of the models listed in Table 3. Ferromagnetic ordering was most stable in all cases and was used when reporting stability and structures in the following.

Fig. 9 compares the DFT stability of various candidate structure models for each of the sample compositions observed in the (S)TEM studies above. The figure compares the total electronic enthalpy per atom. We evaluate enthalpy differences larger than 50 meV/atom to be significant in this respect but note that temperature and entropy effects as well as defects and kinetic barriers can change the relative stability or abundance of the different structural models. It is evident from Fig. 9 that the B2 and $L2_1$ structure models are predicted to be most stable for the Sample A composition. This is in very good

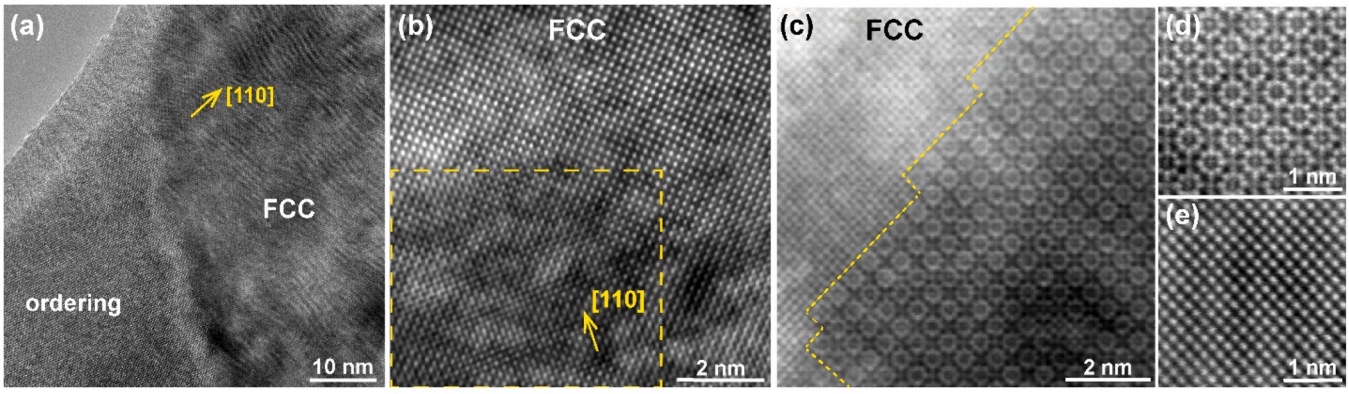

Fig. 5. a) High-resolution TEM image at the interface between FCC and ordered grains in Sample C. Intense moiré fringes are observed only in the FCC phase along the [110] direction. b) Nanoscale phase separation (dashed area) along the [110] direction indicated in high-resolution TEM image of the FCC phase. c) ADF-STEM image of the interface. A coherent relationship between the FCC and the ordered superstructure is revealed, with the phase transition taking place in nano-steps. d)-e) Close-ups of the ordered superstructure and the FCC phase respectively.

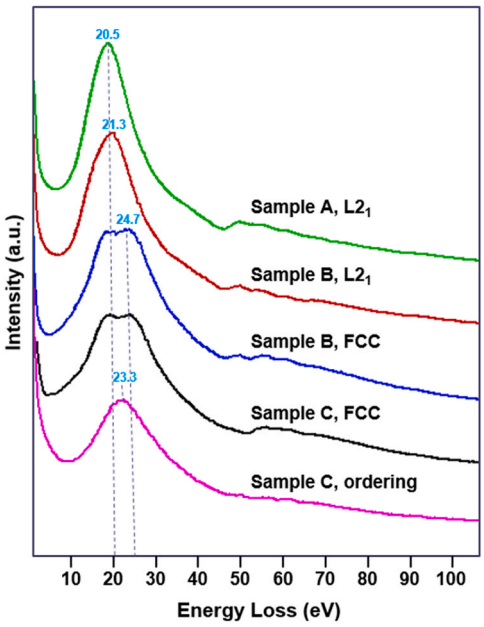

Fig. 6. Comparison of low-loss EELS spectra. A clear plasmon-peak splitting is observed only in the FCC phases indicating two valence electron densities - consistent with the observed phase separation tendency. The phenomenon is suppressed in all ordered phases and a gradual blue-shift takes place by decreasing x (Samples A to C).

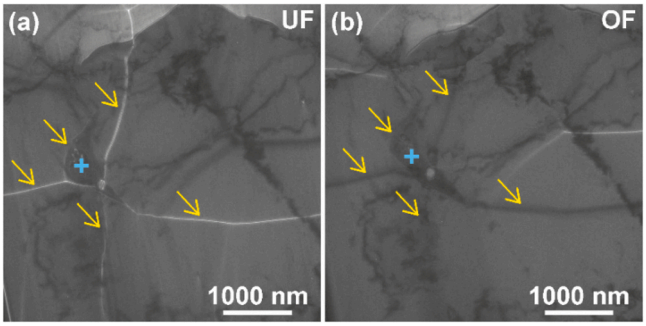

Fig. 7. Lorentz TEM Fresnel images a) underfocused and b) overfocused, acquired close to the ordered grain (annotated by blue cross) in Sample C. Magnetic domain walls (annotated by yellow arrows) were detected due to the alternating contrast (bright-dark). The ordered grains exist at the intersection of magnetic domain walls, hence acting as pinning points for the magnetic domain wall movement.

agreement with the TEM experimental observations, where the coexistence of B2 and L2$_1$ structures are seen. The modeling suggests that the L2$_1$ model M1, in which Al and Mn occupy distinct crystallographic sites, is the most stable. This complies well with the observation of Al-rich atomic columns observed with high-resolution HAADF-STEM (Fig. 2). The enthalpy difference is, however, too small to exclude the coexistence of the L2$_1$ model M2 and the B2 model M1. After taking into account the configurational entropy effect at 1000 K the trend is still the same since ΔH_{form}-$T\Delta S_{conf}$ is lowest for the L2$_1$ model M1 with the L2$_1$ model M2 and the B2 model M1 following.

Sample B was shown above to be separated into two phases: a dominant dendritic and a secondary interdendritic. In TEM the dominant phase was identified as FCC and the secondary L2$_1$. The latter is in perfect agreement with the DFT results in Fig. 9, which conclude that L2$_1$ is at least 78 meV/atom more stable than the competing models. The two L2$_1$ models (M3 and M4) are too close in energy to be distinguished. It was also not possible to discriminate between the candidate models of the dominant part of sample B, as they were all close in enthalpy values. However, taking into account

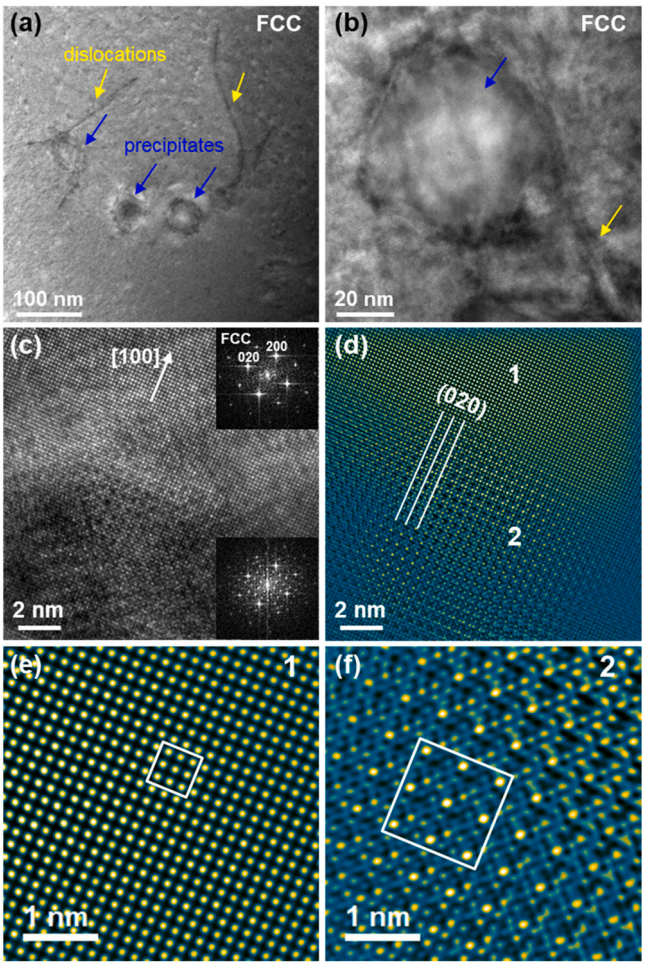

Fig. 8. a) Low-magnification TEM image from Sample C showing pinning of dislocations by nano-sized precipitates. b) A close-up indicates a clear connection of a sharply-faceted nano-precipitate with the dislocation line. c) High-resolution TEM image from a similar nano-precipitate with the corresponding FFTs, showing nanoscale ordering. d) The corresponding IFFT image and e) and f) close-ups of the FCC and the ordered superstructures, respectively. The ordered nano-precipitates exhibit lateral coherency with the surrounding FCC matrix, resulting in a three-times larger cubic unit cell.

the configurational entropy effect at 1000 K, a clear trend towards the disordered phases is observed, with the FCC exhibiting the lowest energy, in accordance with the TEM observations. It is interesting to note that TEM showed that the FCC phase was highly defected and phase-separated. It is likely that such defects are more easily accessible in the unordered FCC structure than in the more ordered competing structures, and that the defects contribute to stabilizing FCC compared to the others.

A similar situation arises in sample C. The DFT results are unable to distinguish between the models because of similar enthalpies, while the disordered FCC structure was seen experimentally to dominate, albeit displaying phase decomposition trends. In this case, an ordered superstructure was also observed, which appears to be another way of stabilizing the structure. The FCC structure is stabilized by the high configurational entropy since calculations again show a clear trend towards the disordered phases for this composition. At this point, we would like to highlight that other entropy contributions except for the configurational one could also be important for determining phase stabilities in HEAs. Ma et al. [77] showed that electronic and magnetic entropies can contribute up to 50% of the configurational entropy value in addition to the vibrational one. Hence, the values of the Gibbs free energy can be slightly different from the ones listed in this work. Furthermore, the actual T

Table 2
Composition of the 48-atom SQS models compared to the experimental composition.

Sample	**A**		**B**		**B**		**C**	
Expt. Phase	**$L2_1$**		**FCC** (dendrite)		**$L2_1$** (interdendr.)		**FCC**	
at%	**Expt.**	**SQS**	**Expt.**	**SQS**	**Expt.**	**SQS**	**Expt.**	**SQS**
Fe	17.1	16.7	29.2	29.2	19.5	18.8	29.3	29.2
Co	16.2	16.7	26.5	27.1	22.1	22.9	29.4	29.2
Ni	17.2	16.7	24.3	25.0	28.9	29.2	31.0	31.3
Al	24.4	25.0	7.1	6.3	16.8	16.7	6.0	6.3
Mn	25.2	25.0	12.9	12.5	12.8	12.5	4.3	4.2

Table 3
The different models investigated for each of the compositions are outlined in Table 2. The distribution of atomic species over the different Wyckoff sites of each structure is also listed, and the formation enthalpy ΔH_{form} is listed for each model relative to the most stable one with the same composition. The enthalpies are reported in meV per atom. Models that are not available at the given composition (e.g. because the content of an element is less than required for the model) are indicated by a dash (-) in the table. The corresponding configurational entropy values ΔS_{conf}, as well as ΔH_{form}-$T\Delta S_{conf}$ for T=1000 K, are also listed for each model.

Phase	**Model**	**Wyckoff sites**			**ΔH_{form} (meV)**				**ΔS_{conf} (meV/K)**			
		a	b	c	**A**	**B** dendr.	**B** interd.	**C**	**A**	**B** dendr.	**B** interd.	**C**
BCC		AlCoFeMnNi			178	19	94	2	0.137	0.129	0.135	0.120
B2	**M1**	AlMn	CoFeNi		38	–	–	–	0.077	–	–	–
	M2	AlCoNi	CoFeMnNi		135	0	88	2	0.093	0.089	0.105	0.091
	M3	AlCoFeMnNi	CoFeMnNi		125	22	78	13	0.118	0.125	0.124	0.116
$L2_1$	**M1**	Al	Mn	CoFeNi	0	–	–	–	0.047	–	–	–
	M2	Al	FeMn	CoFeMnNi	26	–	–	–	0.071	–	–	–
	M3	AlCoNi	FeMn	CoFeMnNi	–	6	12	0	–	0.086	0.076	0.077
	M4	AlMn	CoFeMnNi	AlCoFeNi	–	–	0	–	–	–	0.059	–
FCC		AlCoFeMnNi			161	1	82	13	0.137	0.129	0.135	0.120

ΔH_{form}-$T\Delta S_{conf}$ (meV) @ 1000 K			
A	**B** dendr.	**B** interd.	**C**
41	-110	-41	-118
-39	–	–	–
42	-89	-17	-89
7	-103	-46	-103
-47	–	–	–
-45	–	–	–
–	-80	-64	-77
–	–	-59	–
24	-128	-53	-107

of formation of the primary phases can deviate from the one postulated for our calculations (1000 K).

Table 4 shows the average magnetic moment of each transition metal atom, as well as the total magnetic moment with respect to the total number of atoms in the unit cell and the number of transition metals in the unit cell (#TM). Interestingly, manganese displays the largest magnetic moment in all the phases with μ~3 μ_B. It is closely followed by iron, except in phase A where iron has the lowest μ among the transition metals (it varies between 0 and 0.8 μ_B and averages to 0.3 μ_B). This very low value is particular for Model 1 of the $L2_1$ structure, in which the eight nearest neighbors of Fe, Co, and Ni are four Al and four Mn atoms. This serves to reduce the magnetic moment of all these three elements, compared with all other models – including $L2_1$ Model 2, which exhibits very similar values to the other models in Table 4 (not shown). The magnetic moment of cobalt is approximately 1.5 μ_B, again with phase A as an exception (~1 μ_B). Nickel has the lowest magnetic moment with μ~0.5 μ_B for all phases. These results correlate well with the magnetic moment in the standard bulk phases of the element, except in the case of Mn, which has around twice as high a magnetic moment

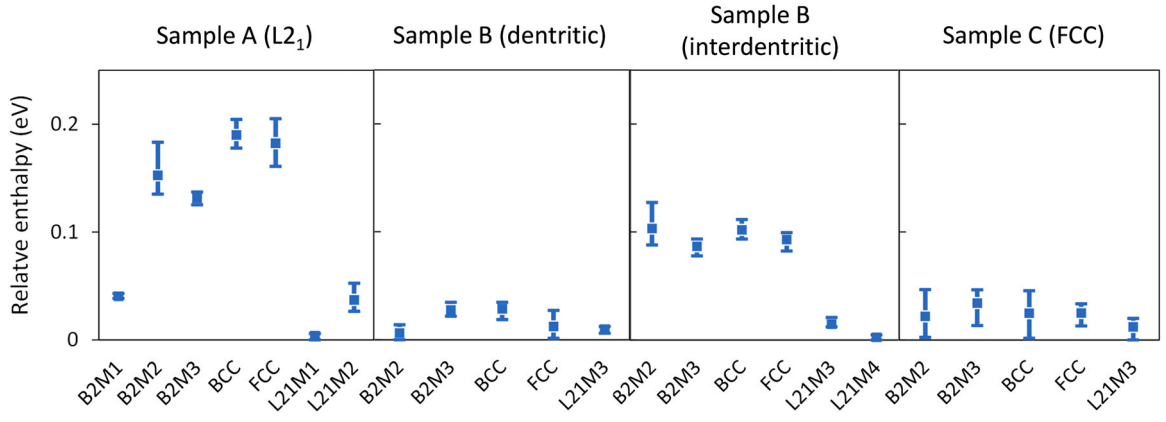

Fig. 9. The DFT calculated relative enthalpy of the various models, in eV per atom. The lowest enthalpy is taken as the zero point for each sample composition. The spread in enthalpy throughout the five SQS arrangements is designated by the vertical line, and the square indicates the average value. The names of the models correspond to those in Table 3.

Table 4
The average magnetic moment per atom in Bohr magnetons (μ_B) calculated by DFT, using the most stable structure (see Table 3 and Fig. 9) in the calculation. It is given for each of the transition metals (TM), the average per atom (including Al), and the average per TM atom. The last column gives the mass magnetization in Am^2kg^{-1}. All the structures were found to be ferromagnetic, which is the only result shown in the table. Also shown is the corresponding magnetic moment of the elements in their standard state. In the case of elemental Mn, the absolute value of single magnetic moments is shown (the total magnetic moment is zero because of the paramagnetic nature of Mn).

Sample	Mn	Fe	Co	Ni	Tot/atom	Tot/#TM	Magn. (Am^2/kg)
A ($L2_1$)	2.80	0.30	0.95	0.43	0.97	1.30	110
B (FCC)	2.87	2.55	1.43	0.57	1.63	1.73	164
B ($L2_1$)	3.27	2.79	1.41	0.47	1.39	1.66	148
C (FCC)	2.82	2.56	1.56	0.56	1.49	1.59	149
Element	1.43	2.27	1.6	0.62	–	–	–

in the HEA phases than in bulk, elemental Mn. The high values of Mn may partially be understood by its nearest neighbors, which consist of a majority of non-Mn atoms, thus exhibiting a different local symmetry than that of bulk Mn. Some models feature Mn atoms with a larger number of Mn nearest neighbors, but they tend to be less stable.

Since the aluminum content varies between the phases, it can be expected that the total magnetic moment per atom varies. Indeed, it is lowest for phase A (~1 μ_B per atom) where the Al content is around 25 at%, while the maximum value is 1.6 μ_B for phase B (FCC) which contains around 6 at% Al. But this is not only a direct effect of the Al content; the magnetic moment per transition metal is also higher in phase B than in phase A. This is caused by the reduced magnetic moment of Fe and Co in phase A as compared to the "standard" bulk values seen in the other phases. Nevertheless, the increased magnetic moment of Mn compared to that of bulk Mn, makes the average magnetic moment per atom relatively high, even when taking into account the Al content.

3.4. Magnetic properties

The magnetic hysteresis loops of the three samples measured at room temperature are presented in Fig. 10. The saturation magnetization (M_s) and coercivity (H_c) values for each sample are also shown in the plots. All alloys were easily magnetized to the saturated state with H_c values below 1000 A/m, indicating that all exhibit good soft magnetic properties.

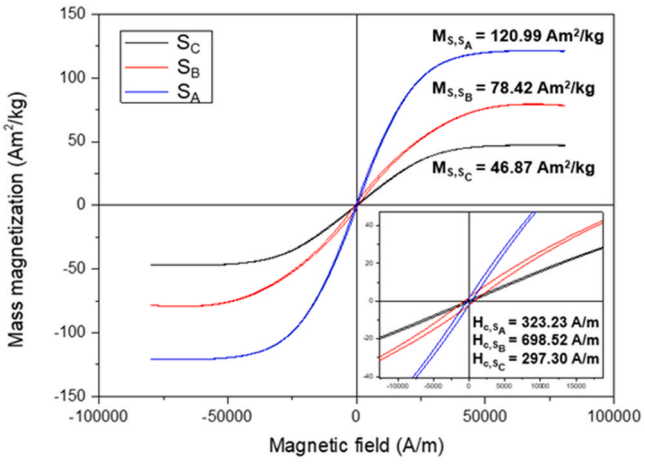

Fig. 10. Hysteresis loops and values of the saturation magnetization (mass) M_s and coercivity H_c (inset) for Sample A (S_A), Sample B (S_B), and Sample C (S_C).

4. Discussion

In our study, a combination of advanced (S)TEM-EELS investigations along with DFT calculations was applied to unravel the structural evolution of $FeCoNi(AlMn)_x$ HEAs at the nano-scale and elucidate its impact on magnetic properties. Previous studies based on microstructural characterization with XRD-SEM, along with theoretical models based on the hypothesis that configurational entropy may favor single-phase solid solution (SS) (as BCC, FCC, HCP), have been proved quite misleading. Miracle and Senkov [11] presented a review of data that do not support an observable effect of configurational entropy on preferred formation of SS phases, triggering the need for advanced nano-scale studies.

Starting with the high Al, Mn-content alloy $FeCoNi(AlMn)_{1.5}$, a chemically-ordered intermetallic compound (IM) was identified with the Heusler structure ($L2_1$) being dominant. Furthermore, a nano-scale interplay between ordered $L2_1$ and B2 was revealed, also supported by DFT results, where the $L2_1$ and B2 structure-models are predicted to be the most stable, exhibiting the lowest relative enthalpy values. The STEM/DFT analysis went one step further in terms of unraveling the elemental occupancy of distinct atomic sites. The most stable $L2_1$ model suggests that Al and Mn occupy the a and b Wyckoff sites, while Fe, Co, Ni occupy the c sites. The highest Al, Mn-content alloy reported previously is the equimolar $FeCoNi(AlMn)_1$, where BCC or B2 or a mixture of BCC/B2 were reported according to XRD studies [29,31,32,36]. Also, Yang et al. [30], Hariharan et al. [32], and Karati et al. [78] showed that the B2 ordered phase is metastable, and an order-disorder transition takes place upon heat treatment.

Although our (S)TEM/DFT results showed a highly-ordered $FeCoNi(AlMn)_{1.5}$ alloy from meso- and down to atomic-scale, it exhibited good soft magnetic behavior (the second-best reported for the high Al, Mn-concentrations, see Table 5) and better M_s than the disordered counterparts (Sample B and C). Since Heusler alloys possess highly-ordered crystal structures in which different elements occupy specific lattice sites, a possible explanation is that the magnetic performance of ordered alloys with similar compositions to HEAs is associated with the specific chemical environment of different elements in the structure (also suggested by Zuo et al. [36]). Furthermore, by adding high-content of non-magnetic elements (as Al) to the FeCoNiMn-base alloy, decreasing trends in the magnetization should be expected, due to the reduction of the mass fraction of total magnetic elements. However, an enhancement in the M_s was measured by VSM, and DFT showed that Mn exhibited the highest magnetic moment in all compositions and enhanced magnetic moment in comparison to that of bulk Mn. This is attributed to the synergistic effect of Mn-Al, since the addition of Al into FeCoNiMn alloy reduces the number of down-spins for Mn, resulting in a switch from the antiferromagnetic to ferromagnetic order, hence leading to an increase of the total magnetic moment of the alloy (as also discussed by Zuo et al. [36] and Zhang et al. [79]).

Reduction in the Al, Mn-content ($FeCoNi(AlMn)_{0.65}$) resulted in the formation of dendritic and interdendritic areas (Sample B). The Fe, Mn-rich dendrites were FCC phase, while the Al, Ni-rich interdendritic phase was ordered $L2_1$. The latter is in perfect agreement with the DFT results, concluding clearly that $L2_1$ is the expected phase in comparison to the other competing models for the measured composition. Regarding the FCC phase identified in Samples B and C, (S)TEM imaging in combination with low-loss EELS revealed a more complicated picture in comparison to what has been reported so far. Reduction in Al, Mn-content results in a gradual phase change from $L2_1$ to an FCC phase. However, although FCC is disordered and has a lower content of 'impurity' Mn and Al elements in the FeCoNi-host, it is not the most stable. A strong phase separation tendency at the nanoscale was observed in the FCC phase of both Samples B and C. This trend is very clear by comparing the FCC dendritic and $L2_1$

Table 5
Magnetic properties of as-cast FeCoNi(AlMn)$_x$ HEAs measured in this work compared to previously reported values. Results are presented by decreasing x.

Alloy	Method	M_s (Am^2/kg)	H_c (A/m)	Ref.
FeCoNi(AlMn)$_{1.5}$	laser metal deposition	121	323	This work
FeCoNi(AlMn)$_1$	vacuum arc melting	126	533	Hariharan et al.[32]
FeCoNi(AlMn)$_1$	arc melting	125	95	Li et al.[29]
FeCoNi(AlMn)$_1$	magnetic levitation induction melting	118	576	Yang et al.[30]
FeCoNi(AlMn)$_1$	arc melting	148	629	Zuo et al.[37]
FeCoNi(AlMn)$_{0.65}$	laser metal deposition	78	699	This work
FeCoNi(AlMn)$_{0.5}$	arc melting	50	187	Li et al.[29]
FeCoNi(AlMn)$_{0.25}$	vacuum arc melting	101	268	Li et al.[27]
FeCoNi(AlMn)$_{0.25}$	arc melting	99	493	Lu et al.[31]
FeCoNi(AlMn)$_{0.2}$	laser metal deposition	47	297	This work
FeCoNi(AlMn)$_{0.1}$	arc melting	140	126	Li et al.[29]

interdendritic phases in Sample B. High-resolution imaging revealed intense moiré fringes and high defect-density in the FCC phase, while the moiré fringes disappeared in the L2$_1$ phase that was defect-free. Low-loss EELS revealed plasmon-peak splitting only in the disordered FCC phase, indicative of the existence of two valence-electron states. Interestingly, this phenomenon was eliminated in all ordered phases detected in all samples, regardless of the composition. DFT was not possible to discriminate between candidate models for compositions where FCC was identified with TEM, since all suggested models exhibited similar enthalpies. By taking into account the configurational entropy effect at 1000 K, ΔH_{form}-$T\Delta S_{conf}$ indicates that disordered phases (FCC or BCC) are more stable than the ordered L2$_1$ and B2 models at the corresponding compositions. However, the differences are small, and electronic and magnetic entropy contributions can also be important for determining phase stability in HEAs [77]. Furthermore, the actual T of formation of the primary phases can deviate from the one postulated for our calculations (1000 K).

All samples in our study exhibit good soft magnetic properties since they were easily magnetized to the saturated state with coercivity values H_c below 1000 A/m. The value of saturation magnetization M_s decreases considerably as the alloy moves away from the classical HEA equimolar composition (moving from Sample A to Sample C). This is in line with previous results reporting that M_s is affected by changes in the chemical composition. Li et al. [29] suggested that the value of M_s increases when the Mn mole fraction exceeds 12.5% in FeCoNiAlMn HEAs.

Our DFT results showed that Mn atoms carry the highest local magnetic moment and Alijani et al. [45] suggested that Mn atoms together with Co define the magnetic behavior of Fe. Furthermore, the synergistic effect between the antiferromagnetic Mn and non-magnetic Al as mentioned above, leads to an increase of the total magnetic moment of the alloy, explaining the high M_s values observed in Sample A.

Regarding the saturation magnetization M_s, Zhang et al. [80] reported that it is highly dependent on the crystal structure and composition of HEAs and Shyni et al. [81] showed that it is less sensitive to the grain size of the material. However, it may be affected by the change in grain connectivity, i.e., the microstructure of the material. Furthermore, when dealing with HEAs, one should also take into account that the chemical short-range order in these systems significantly changes the local environment and can further affect the average magnetic moment of the material (Feng et al. [82]). The M_s measured in Sample C is lower than the reported results for low Al, Mn-contents. This can indicate that the chemically ordered nano-precipitates and ordered grains that nucleated mainly along grain-boundaries in the FCC phase play a crucial role in grain connectivity and can be the main factors for the reduced M_s. Furthermore, despite the FCC phase being dominant in Sample C, the intense phase separation trends may also have an impact on the M_s reduction. The DFT predicted magnetization values are in the same range as the measured M_s of sample A, indicating that the SQS models give a good description of that sample. However, the M_s of the other samples is not well reproduced by the DFT calculations. This may be due to the reduction of M_s in those samples as described above; in that case, the DFT values identify theoretical maximum values given samples with fewer defects. Also, there is a possibility that ferrimagnetic ordering reduces the overall magnetization -the enormous number of possible ferrimagnetic permutations makes it intractable to investigate all eventualities-, so unrevealed stable ferrimagnetic phases cannot be ruled out.

Concerning the H_c values, the existence of dendritic FCC and interdendritic L2$_1$ areas in Sample B indicates the existence of long phase boundaries. Phase boundaries make the movement of magnetic domain walls difficult, justifying the higher H_c values in comparison to the other samples (Qu et al. [83]). In Sample C, pinning of magnetic domain walls and dislocations by ordered precipitates was revealed by STEM imaging and Lorentz TEM. Hindering of the magnetic domain wall movement and lattice distortions are expected to increase H_c [84,85]. However, H_c values of Sample C were just slightly lower than Sample A. Taking into account that grain size is also an important factor affecting H_c and Sample A exhibits sub-grain structure as presented in our previous work [69], this could lead to higher coercivity than in Sample C, despite the pinning by the ordered nano-precipitates. Finally, the density of the ordered nano-precipitates in Sample C was low, hence the pinning process did not play the dominant role in affecting magnetic properties.

Phase separation trends have been reported before in HEAs, such as spinodal decomposition, ordering, and precipitation, mainly in spatially confined and segregated regions, mostly creating side effects outside of the target mechanical and magnetic properties [1,54,57,58,86,87]. However, recently Rao et al. [55] exploited the metastability of these alloys, triggering bulk spinodal decomposition for improving the alloys' magnetic properties. In particular, they showed that atomic-scale decomposition of FeCoNiMnCu into two regions (Fe, Co-enriched, and Cu-enriched) after annealing at 700 °C resulted in enhanced magnetization in comparison to the single-phase bulk-like material of the same composition. Similarly, our FeCoNi(AlMn)$_{0.2}$ alloy exhibits a metastable FCC phase, with a phase decomposition tendency indicated by the intense moiré fringes and the existence of two valence electron concentrations (plasmon-peak splitting in low-loss EELS). The decomposition takes place along the [110] direction (Fig. 4a) and atomic-scale EDX maps did not reveal a detectable chemical trend, indicating that chemical fluctuations were still small. This trend offers a great platform to study the effect of phase separation in the magnetic behavior of the FeCoNiAlMn system. Since FeCoNi(AlMn)$_{0.2}$ already exhibits good soft magnetic properties, the next step in our study is to trigger spinodal decomposition by thermal annealing, resulting in nanoscale isostructural chemical decompositions. In this respect, in-situ heating experiments in STEM will be crucial in monitoring the real-time bulk spinodal decomposition of FeCoNi(AlMn)$_{0.2}$ at the near-atomic level

and finally enhance the magnetic properties of the alloy by chemically designing the appropriate spinodal regime.

5. Conclusion

In our study, a detailed nanoscale investigation of high-entropy $FeCoNi(AlMn)_x$ alloys processed by laser metal deposition was conducted, by combining imaging and spectroscopies in (scanning) transmission electron microscopy along with DFT calculations. The structural evolution of the alloy by varying its chemical composition ($0.2 \leq x \leq 1.5$) was elucidated, revealing a gradual change of the face-centered cubic (FCC) towards an ordered full-Heusler ($L2_1$) phase by increasing the Al and Mn content. Although the high entropy effect is supposed to greatly enhance the formation of solid solution phases, here we report the stabilization of chemically-ordered intermetallic compounds in the case of high Al, Mn contents. In particular, a co-existence on the nano-scale of two ordered structures, B2 and $L2_1$, is reported for the first time in the FeCoNiAlMn system. Atomic-site occupancy of $L2_1$ was resolved by direct imaging and atomic-scale calculations, with Al and Mn occupying the a and b Wyckoff sites respectively. Ordering phenomena as superstructures of nano-precipitates and nano-sized grains were also detected in the FCC phase for low Al, Mn contents, acting as pinning-sites for the movement of magnetic domain walls and dislocations. Furthermore, the FCC phase exhibits a strong phase decomposition tendency as indicated by the intense moiré fringes and the existence of two valence electron concentrations shown by low-loss EELS. The alloys in the whole compositional range exhibited good soft-magnetic behavior since they were easily magnetized to the saturated state with coercivity values of < 1000 A/m. The formation of the intermetallic $L2_1$/B2 nanostructure -instead of a solid solution- did not have a negative effect on the soft magnetic properties, indicating that the magnetic performance of ordered alloys with similar compositions to HEAs is more associated with the specific chemical environment of distinct elements occupying specific lattice-sites. Mn displayed the largest magnetic moment in all phases and $FeCoNi(AlMn)_{1.5}$ exhibited the highest saturation magnetization M_s, attributed to the synergistic effect of Mn-Al. Phase separation trends seem to decrease the M_s, however, the overall impact on the magnetic behavior of the alloy is not intense, opening up for new avenues for tuning FeCoNiAlMn properties through chemically-designed phase decomposition regimes.

CRediT authorship contribution statement

C. Bazioti: Conceptualization, Methodology, Investigation ((S)TEM, EDX, EELS), Visualization, Writing – original draft, Writing – review & editing. **O.M. Løvvik**: Methodology, Investigation (DFT), Visualization, Writing – original draft, Writing – review & editing, Funding acquisition. **A. Poulia**: Methodology, Investigation (SEM, XRD, VSM), Visualization, Writing – original draft. **P.A. Carvalho**: Writing – review & editing, Funding acquisition. **A.S. Azar**: Methodology (LMD), Resources, Funding acquisition. **P. Mikheenko**: Writing – review & editing, Supervision, Resources, Funding acquisition. **S. Diplas**: Writing – review & editing, Supervision, Resources, Funding acquisition, Project administration. **A.E. Gunnæs**: Writing – review & editing, Supervision, Resources, Funding acquisition.

Declaration of Competing Interest

The authors declare that they have no known competing financial interests or personal relationships that could have appeared to influence the work reported in this paper.

Acknowledgments

This work is part of the Project “MAGNIFICENT - Additively manufactured magnetic high entropy alloys for renewable electricity”, funded by the Research Council of Norway (no. 287979) within the NANO2021 Program. The Research Council of Norway is also acknowledged for support to the Norwegian Center for Transmission Electron Microscopy (NORTEM) (no. 197405/F50). Computational resources were provided by Sigma2 through grant no. nn2615k. The authors would also like to express their appreciation to Petter Silkoset, Pavel Doubrovin and, Evgeniy Kulakov from the Ivar Giæver Geomagnetic Laboratory, Department of Geosciences, University of Oslo, Norway for their assistance in the VSM experiments.

References

[1] J.W. Yeh, S.K. Chen, S.J. Lin, J.Y. Gan, T.S. Chin, T.T. Shun, C.H. Tsau, S.Y. Chang, Nanostructured high-entropy alloys with multiple principal elements: novel alloy design concepts and outcomes, Adv. Eng. Mater. 6 (2004) 299–303.
[2] B. Cantor, I.T.H. Chang, P. Knight, A.J.B. Vincent, Microstructural development in equiatomic multicomponent alloy, Mater. Sci. Eng. A 375 (2004) 213–218.
[3] B.S. Murty, J.W. Yeh, S. Ranganathan, P.P. Bhattacharjee, Matthew deans, High-entropy Alloys, second ed., Elsevier, 2019.
[4] M.C. Gao, J.W. Yeh, P.K. Liaw, Y. Zhang, High-entropy Alloys: Fundamentals and Applications, first ed., Springer International Publishing, 2016.
[5] X.D. Xu, P. Liu, S. Guo, A. Hirata, T. Fujita, T.G. Nieh, C.T. Liu, M.W. Chen, Nanoscale phase separation in a fcc-based $CoCrCuFeNiAl_{0.5}$ high-entropy alloy, Acta Mater. 84 (2015) 145–152.
[6] T. Wang, S. Shukla, M. Komarasamy, K. Liu, R.S. Mishra, Towards heterogeneous $Al_xCoCrFeNi$ high entropy alloy via friction stir processing, Mater. Lett. 236 (2019) 472–475.
[7] Z. Li, C.X. Wang, L.Y. Yu, Y. Gu, M.X. Pan, X.H. Tan, H. Xu, Magnetic properties and microstructure of $FeCoNi(CuAl)_{0.8}Sn_x$ ($0 \leq x \leq 0.10$) high-entropy alloys, Entropy 20 (2018) 872.
[8] C. Zlotea, M.A. Sow, G. Ek, J.P. Couzinie, L. Perriere, I. Guillot, J. Bourgon, K.T. Møller, T.R. Jensen, E. Akiba, M. Sahlberg, Hydrogen sorption in TiZrNbHfTa high entropy alloy, J. Alloy. Compd. 775 (2019) 667–674.
[9] C. Jung, K. Kang, A. Marshal, K.G. Pradeep, J.-B. Seol, H.M. Lee, P.-P. Choi, Effects of phase composition and elemental partitioning on soft magnetic properties of AlFeCoCrMn high entropy alloys, Acta Mater. 171 (2019) 31–39.
[10] P.A. Ibrahim, İ. Özkul, C.A. Canbay, An overview of high-entropy alloys, Emergent Materials, Article in press.
[11] D.B. Miracle, O.N. Senkov, A critical review of high entropy alloys and related concepts, Acta Mater. 122 (2017) 448–511.
[12] V.E. Gromov, S.V. Konovalov, Yu.F. Ivanov, K.A. Osintsev, Structure and Properties of High-Entropy Alloys, Part of the Advanced Structured Materials book series (STRUCTMAT) volume 107, Springer Nature, Switzerland AG, 2021, p. 2021.
[13] Y. Zhang, D. Wang, S. Wang, Review: High-entropy alloys for electrocatalysis: Design, characterization, and applications, Small 18 (2022) 2104339.
[14] Q. Ding, Y. Zhang, X. Chen, X. Fu, D. Chen, S. Chen, L. Gu, F. Wei, H. Bei, Y. Gao, M. Wen, J. Li, Z. Zhang, T. Zhu, R.O. Ritchie, Q. Yu, Tuning element distribution, structure and properties by composition in high-entropy alloys, Nature 574 (2019) 223–227.
[15] Z.F. Lei, X.J. Liu, Y. Wu, H. Wang, S.H. Jiang, S.D. Wang, X.D. Hui, Y.D. Wu, B. Gault, P. Kontis, D. Raabe, L. Gu, Q.H. Zhang, H.W. Chen, H.T. Wang, J.B. Liu, K. An, Q.S. Zeng, T.G. Nieh, Z.P. Lu, Enhanced strength and ductility in a high-entropy alloy via ordered oxygen complexes, Nature 563 (2018) 546–550.
[16] W. Zhang, M. Zhang, Y. Peng, F. Liu, Y. Liu, S. Hu, Y. Hu, Effect of Ti/Ni coating of diamond particles on microstructure and properties of high-entropy alloy/diamond composites, Entropy 21 (2019) 164.
[17] S.S. Nene, S. Sinha, M. Frank, K. Liu, R.S. Mishra, B.A. McWilliams, K.C. Cho, Unexpected strength-ductility response in an annealed, metastable, high-entropy alloy, Appl. Mater. Today 13 (2018) 198–206.
[18] O. Senkov, G.B. Wilks, J.M. Scott, D.B. Miracle, , Mechanical properties of $Nb_{25}Mo_{25}Ta_{25}W_{25}$ and $V_{20}Nb_{20}Mo_{20}Ta_{20}W_{20}$ refractory high entropy alloys, Intermetallics 19 (2011) 698–706.
[19] B. Gludovatz, A. Hohenwarter, D. Catoor, E.H. Chang, E.P. George, R.O. Ritchie, A fracture-resistant high-entropy alloy for cryogenic applications, Science 345 (2014) 1153–1158.
[20] P. Wu, K. Gan, D. Yan, Z. Li, The temperature dependence of deformation behaviors in high-entropy alloys: A review, Metals 11 (2021) 2005.
[21] R. Motallebi, Z. Savaedi, H. Mirzadeh, Superplasticity of high-entropy alloys: A review, Civ. Mech. Eng. 22 (2022) 1–14.
[22] S. Singh, N. Wanderka, K. Kiefer, K. Siemensmeyer, J. Banhart, Effect of decomposition of the Cr-Fe-Co rich phase of AlCoCrCuFeNi high entropy alloy on magnetic properties, Ultramicroscopy 111 (6) (2011) 619–622.
[23] P. Koˇzelj, S. Vrtnik, A. Jelen, S. Jazbec, Z. Jagliˇci´c, S. Maiti, M. Feuerbacher, W. Steurer, J. Dolinˇsek, Discovery of a superconducting high-entropy alloy, Phys. Rev. Lett. 113 (2014) 107001.
[24] M. Fu, X. Ma, K. Zhao, X. Li, D. Su, High-entropy materials for energy-related applications, iScience 24 (2021) 102177.
[25] X. Wang, W. Guo, Y. Fu, High-entropy alloys: emerging materials for advanced functional applications, J. Mater. Chem. A 9 (2021) 663–701.

[26] T.V. Jayaraman, A. Rathi, G.V. Thotakura, Phase evolution, structure, and magnetic characterization of mechanosynthesized $Co_{40}Fe_{30}Ni_{30}$ medium-entropy alloy, Intermetallics 113 (2019) 106583.
[27] P.P. Li, A.D. Wang, C.T. Liu, A ductile high entropy alloy with attractive magnetic properties, J. Alloy. Compd. 694 (2017) 55–60.
[28] Y. Duan, M. Gao, H. Pang, T. Wang, FeCoNiMnAl high-entropy alloy: Improving electromagnetic wave absorption properties, J. Mater. Res. 36 (10) (2021) 2107–2117.
[29] Z. Li, G. Bai, X. Liu, S. Bandaru, Z. Wu, X. Zhang, M. Yan, H. Xu, Tuning phase constitution and magnetic properties by composition in FeCoNiAlMn high-entropy alloys, J. Alloy. Compd. 845 (2020) 156204.
[30] C. Yang, J. Zhang, M. Li, X. Liu, Soft-magnetic high-entropy AlCoFeMnNi alloys with dual-phase microstructures induced by annealing, Acta Metal. Sin. (Engl. Lett.) 33 (2020) 1124–1134.
[31] T. Lu, T. He, P. Zhao, K. Sun, A.F. Andreoli, H. Chen, W. Chen, Z. Fu, S. Scudino, Fine tuning in-sync the mechanical and magnetic properties of $FeCoNiAl0_{.25}Mn_{0.25}$ high-entropy alloy through cold rolling and annealing treatment, J. Mater. Proc. Tech. 289 (2021) 116945.
[32] V.S. Hariharan, A. Karati, T. Parida, R. John, D.A. Babu, B.S. Murty, Effect of Al addition and homogenization treatment on the magnetic properties of CoFeMnNi high-entropy alloy, J. Mater. Sci. 55 (2020) 17204–17217.
[33] Y. Duan, X. Sun, Z. Li, G. Ma, Q. Yu, G. Wei, L. Huang, X. Wang, H. Pang, X. Liu, High frequency magnetic behavior of $FeCoNiMn_xAl_{1-x}$ high-entropy alloys regulated by ferromagnetic transformation, J. Alloy. Compd. 900 (2022) 163428.
[34] M. Zhang, L. Yao, M. Zhu, Y. Liu, Z. Jian, Structural evolution and mechanical and magnetic properties of nonequiatomic $CoFe_2NiMn_{0.3}Al_x$ ($0.25 \le x \le 1.00$) high-entropy alloys, J. Mater. Eng. Perform. 30 (2) (2021) 1472–1478.
[35] M.S. Lucas, L. Mauger, J.A. Munoz, Y.M. Xiao, A.O. Sheets, S.L. Semiatin, J. Horwath, Z. Turgut, Magnetic and vibrational properties of high-entropy alloys, J. Appl. Phys. 109 (2011) 3.
[36] T.T. Zuo, R.B. Li, X.J. Ren, Y. Zhang, Effects of Al and Si addition on the structure and properties of CoFeNi equal atomic ratio alloy, J. Magn. Magn. Mater. 371 (2014) 60–68.
[37] T. Zuo, M.C. Gao, L. Ouyang, X. Yang, Y. Cheng, R. Feng, S. Chen, P.K. Liaw, J.A. Hawk, Y. Zhang, Tailoring magnetic behavior of CoFeMnNiX (X = Al, Cr, Ga, and Sn) high entropy alloys by metal doping, Acta Mater. 130 (2017) 10–18.
[38] C. Chen, W. Wang, H. Li, P. Wei, W. Zhang, Y. Fan, J. Chen, S. Yuan, R. Wei, T. Zhang, J. Jiang, T. Wang, F. Li, Effects of Al and Mn on microstructure, magnetic and mechanical properties of $Fe_{40}Co_{40}Ni_{10}M_{10}$ (M=Al, Mn) medium entropy alloys, J. Alloy. Compd. 890 (2021) 161779.
[39] T. Chang, C.M. Zou, D.D. Zhu, X.H. Wang, Z.J. Wei, H.W. Wang, N. Fang, J.H. Chen, Microstructure and magnetic behaviors of FeCoNi (Al) alloys with incoherent nanoprecipitates prepared by high-pressure solidification, J. Alloy. Compd. 894 (2022) 162501.
[40] W. Feng, Y. Qi, S. Wang, Effects of Mn and Al addition on structural and magnetic properties of FeCoNi-based high entropy alloys, Mater. Res. Express 5 (2018) 106511.
[41] S.K. Shaw, A. Gangwar, A. Sharma, S.K. Alla, S. Kavita, M. Vasundhara, S.S. Meena, P. Maiti, N.K. Prasad, Structural and magnetic properties of nanocrystalline equiatomic spinel high-entropy oxide $(AlCoFeMnNi)_3O_4$ synthesised by microwave assisted co-precipitation technique, J. Alloy. Compd. 878 (2021) 160269.
[42] Z. Li, J. Qi, Z. Li, H. Li, H. Xu, G. Bai, X. Liu, X. Zhang, Effect of grain and phase boundaries on soft magnetic properties of FeCoNiAlSi high-entropy alloys, Mater. Lett. 297 (2021) 129965.
[43] C.-L. Lin, T.-W. Chen, Y.-J. Chang, H. Murakami, S. Mitani, A.C. Yeh, Dimensional stability of a metastable FCC high entropy alloy, Appl. Phys. Lett. 119 (2021) 171902.
[44] R. Kulkarni, B.S. Murty, V. Srinivas, Study of microstructure and magnetic properties of AlNiCo(CuFe) high entropy alloy, J. Alloy. Compd. 746 (2018) 194–199.
[45] V. Alijani, J. Winterlik, G.H. Fecher, S.S. Naghavi, C. Felser, Quaternary half-metallic Heusler ferromagnets for spintronics applications, Phys. Rev. B 83 (2011) 184428.
[46] A.F. Andreoli, J. Orava, P.K. Liaw, H. Weber, M.F. Oliveira, K. Nielsch, I. Kaban, The elastic-strain energy criterion of phase formation for complex concentrated alloys, Materialia 5 (2019) 100222.
[47] Y. Zhang, Y.J. Zhou, Solid solution formation criteria for high entropy alloys, Mater. Sci. Forum 561 (2007) 1337–1339.
[48] Y. Zhang, Y.J. Zhou, J.P. Lin, G.L. Chen, P.K. Liaw, Solid-solution phase formation rules for multi-component alloys, Adv. Eng. Mater. 10 (2008) 534–538.
[49] F. Otto, Y. Yang, H. Bei, E.P. George, Relative effects of enthalpy and entropy on the phase stability of equiatomic high-entropy alloys, Acta Mater. 61 (2013) 2628–2638.
[50] O.N. Senkov, D.B. Miracle, A new thermodynamic parameter to predict formation of solid solution or intermetallic phases in high entropy alloys, J. Alloy. Compd. 658 (2016) 603–607.
[51] S. Guo, C. Ng, J. Lu, C.T. Liu, Effect of valence electron concentration on stability of fcc or bcc phase in high entropy alloys, J. Appl. Phys. 109 (2011) 103505.
[52] Z. Rao, A. Çakır, Ö. Özgün, D. Ponge, D. Raabe, Z. Li, M. Acet, 3d Transition-metal high-entropy Invar alloy developed by adjusting the valence-electron concentration, Phys. Rev. Mater. 5 (2021) 044406.
[53] X. Chang, M. Zeng, K. Liu, L. Fu, Phase engineering of high-entropy alloys, Adv. Mater. 32 (2020) 1907226.
[54] F. Sun, G. Miyamoto, Y. Liu, Y. Hayasaka, T. Furuhara, Phase separation with ordering in aged Fe-Ni-Mn medium entropy alloy, Acta Mater. 223 (2022) 117487.
[55] Z. Rao, B. Dutta, F. Körmann, W. Lu, X. Zhou, C. Liu, A. Kwiatkowski da Silva, U. Wiedwald, M. Spasova, M. Farle, D. Ponge, B. Gault, J. Neugebauer, D. Raabe, Z. Li, Beyond solid solution high-entropy alloys: Tailoring magnetic properties via spinodal decomposition, Adv. Funct. Mater. 31 (2021) 2007668.
[56] J.E. Morral, S. Chen, Stability of high entropy alloys to spinodal decomposition, J. Phase Equilib. Diffus. 42 (2021) 673–695.
[57] L. Li, Z. Li, A.K. da Silva, Z. Peng, H. Zhao, B. Gault, D. Raabe, Segregation-driven grain boundary spinodal decomposition as a pathway for phase nucleation in a high-entropy alloy, Acta Mater. 178 (2019) 1–9.
[58] Y.J. Liang, L. Wang, Y. Wen, B. Cheng, Q. Wu, T. Cao, Q. Xiao, Y. Xue, G. Sha, Y. Wang, High-content ductile coherent nanoprecipitates achieve ultrastrong high-entropy alloys, Nat. Commun. 9 (2018) 4063.
[59] S. Zhao, Effects of local elemental ordering on defect-grain boundary interactions in high-entropy alloys, J. Alloy. Compd. 887 (2021) 161314.
[60] S. Zhao, Role of chemical disorder and local ordering on defect evolution in high-entropy alloys, Phys. Rev. Mater. 5 (2021) 103604.
[61] J.W. Cahn, On spinodal decomposition, Acta Met. 9 (1961) 795–801.
[62] G. Kostorz, Phase Transformations in Materials, Wiley, New York, 2001.
[63] T. Graf, C. Felser, S.S.P. Parkin, Simple rules for the understanding of Heusler compounds, Prog. Solid State Chem. 39 (2011) 1–50.
[64] T. Zuo, Y. Cheng, P. Chen, Z. Gao, Y. Zhang, P.K. Liaw, Structural and magnetic transitions of CoFeMnNiAl high-entropy alloys caused by composition and annealing, Intermetallics 137 (2021) 107298.
[65] S. Sonal, J. Lee, Recent advances in additive manufacturing of high entropy alloys and their nuclear and wear-resistant applications, Metals 11 (2021) 1–47.
[66] A.O. Moghaddam, N.A. Shaburova, M.N. Samodurova, A. Abdollahzadeh, E.A. Trofimov, Additive manufacturing of high entropy alloys: A practical review, J. Mater. Sci. Technol. 77 (2021) 131–162.
[67] Z.U. Arif, M.Y. Khalid, A. Al Rashid, E. ur Rehman, M. Atif, Laser deposition of high-entropy alloys: A comprehensive review, Opt. Laser Technol. 145 (2022) 107447.
[68] C. Han, Q. Fang, Y. Shi, S.B. Tor, C.K. Chua, K. Zhou, Recent advances on high-entropy alloys for 3D Printing, Adv. Mater. 32 (2020) 1903855.
[69] A. Poulia, A.S. Azar, M. Schrade, J.S. Graff, C. Bazioti, A.E. Gunnæs, P.A. Carvalho, S. Diplas, Process-Structure-Property (PSP) Relationship in $FeCoNiAl_xMn_x$ complex concentrated alloys processed by additive manufacturing, J. Mater. Eng. Perform. 30 (8) (2021).
[70] Z. Wang, Y. Huang, Y. Yang, J. Wang, C.T. Liu, Atomic-size effect and solid solubility of multicomponent alloys, Scr. Mater. 94 (2015) 28–31.
[71] D.J.M. King, S.C. Middleburgh, A.G. McGregor, M.B. Cortie, Predicting the formation and stability of single-phase high-entropy alloys, Acta Mater. 104 (2016) 172–179.
[72] G. Kresse, J. Hafner, Abinitio molecular-dynamics for liquid-metals, Phys. Rev. B 47 (1993) 558–561.
[73] G. Kresse, J. Furthmüller, Efficient iterative schemes for ab initio total-energy calculations using a plane-wave basis set, Phys. Rev. B 54 (1996) 11169–11186.
[74] J.P. Perdew, K. Burke, M. Ernzerhof, Generalized gradient approximation made simple, Phys. Rev. Lett. 77 (1996) 3865–3868.
[75] A. Zunger, S.H. Wei, L.G. Ferreira, J.E. Bernard, Special quasirandom structures, Phys. Rev. Lett. 65 (1990) 353–356.
[76] O. Hellman, I.A. Abrikosov, S.I. Simak, Lattice dynamics of anharmonic solids from first principles, Phys. Rev. B 84 (2011) 180301.
[77] D. Ma, B. Grabowski, F. Körmann, J. Neugebauer, D. Raabe, Ab initio thermodynamics of the CoCrFeMnNi high entropy alloy: Importance of entropy contributions beyond the configurational one, Acta Mater. 100 (2015) 90–97.
[78] A. Karati, K. Guruvidyathri, V.S. Hariharan, B.S. Murty, Thermal stability of AlCoFeMnNi high-entropy alloy, Scr. Mater. 162 (2019) 465–467.
[79] B. Zhang, Y. Duan, H. Zhang, S. Huang, G. Ma, T. Wang, X. Dong, N. Jia, Magnetic transformation of Mn from anti-ferromagnetism to ferromagnetism in $FeCoNiZMn_x$ (Z = Si, Al, Sn, Ge) high entropy alloys, J. Mater. Sci. Technol. 68 (2021) 124–131.
[80] Y. Zhang, T.T. Zuo, Y.Q. Cheng, P.K. Liaw, High-entropy alloys with high saturation magnetization, electrical resistivity, and malleability, Sci. Rep. 3 (2013) 1455.
[81] P.C. Shyni, P. Alagarsamy, Effect of annealing on structural and magnetic properties of Al substituted nanocrystalline Fe–Si–Co alloy powders, J. Magn. Magn. Mater. 417 (2016) 62–68.
[82] W.Q. Feng, Y. Qi, S.P. Wang, Effects of Short-range Order on the Magnetic and Mechanical Properties of $FeCoNi(AlSi)_x$ High Entropy Alloys, Metals 7 Basel, 2017, pp. 482–496.
[83] H.Z. Qu, M.L. Gong, F.F. Liu, B.Y. Gao, J. Bai, Q.Z. Gao, S. Li, Microstructure, mechanical properties and magnetic properties of $FeCoNiCuTiSi_x$ high-entropy alloys, Sci. China, Technol. Sci. 63 (3) (2020) 459–466.
[84] Z. Fu, B. MacDonald, Z. Li, Z. Jiang, W. Chen, Y. Zhou, E. Lavernia, Engineering heterostructured grains to enhance strength in a single-phase high entropy alloy with maintained ductility, Mater. Res. Lett. 6 (11) (2018) 634–640.
[85] Z.Q. Fu, B.E. MacDonald, T.C. Monson, B. Zheng, W. Chen, E.J. Lavernia, Influence of heat treatment on microstructure, mechanical behavior, and soft magnetic properties in an fcc-based $Fe_{29}Co_{28}Ni_{29}Cu_7Ti_7$ high-entropy alloy, J. Mater. Res 33 (2018) 2214–2222.
[86] S. Singh, N. Wanderka, B. Murty, U. Glatzel, J. Banhart, Decomposition in multi-component AlCoCrCuFeNi high-entropy alloy, Acta Mater. 59 (1) (2011) 182–190.
[87] Y. Zhang, Z. Chen, D. Cao, J. Zhang, P. Zhang, Q. Tao, X. Yang, Concurrence of spinodal decomposition and nano-phase precipitation in a multi-component AlCoCrCuFeNi high-entropy alloy, J. Mater. Res. Technol. 8 (1) (2019) 726–736.